Chapter 23
Optical and Magnetic Functionalities on Molecule-Based Magnetic Materials

Koji Nakabayashi, Shin-ichi Ohkoshi and Szymon Chorazy

Abstract In this chapter, the optical and magnetic properties of multifunctional cyanido-bridged metal assemblies are introduced. Cyanido-bridged metal assemblies draw much attention due to their magnetic properties and functionalities. As for magnetic properties, they have an advantage to show long-range magnetic ordering due to strong magnetic couplings between magnetic metal ions via cyanide. In addition, the cyanido-bridged metal assemblies can acquire structural diversity and various electronic states by combination of metal ions and ligand, resulted in their functionalities. For examples, introduction of transition metal ions showing charge transfer and spin crossover could allow switching of spin states by external stimuli, and metal assemblies containing lanthanide ions are expected to show luminescence and slow magnetic relaxation. Herein, some cyanido-bridged metal assemblies with unique characters of photoinduced magnetization, luminescence, and slow magnetic relaxation are presented.

23.1 Introduction

Studies on multifunctional materials where various magnetic, electric, and optical properties coexist are of interest in chemistry research [1, 2]. To design multifunctional materials, building blocks, which determine the chemical and physical properties, should be selected appropriately. From the viewpoint of designability, molecule-based materials such as metal complexes have received much attention because different combinations of metal cations and ligands provide various

K. Nakabayashi · S. Ohkoshi (✉)
Department of Chemistry, School of Science, The University of Tokyo, 7-3-1 Hongo, Bunkyo-ku, Tokyo 113-0033, Japan
e-mail: ohkoshi@chem.s.u-tokyo.ac.jp

K. Nakabayashi
e-mail: knakabayashi@chem.s.u-tokyo.ac.jp

S. Chorazy
Faculty of Chemistry, Jagiellonian University, Ingardena 3, 30-060 Kraków, Poland
e-mail: chorazy@chemia.uj.edu.pl

K. Yamanouchi et al. (eds.), *Progress in Photon Science*, Springer Series in Chemical Physics 119, https://doi.org/10.1007/978-3-030-05974-3_23

structures and desirable functionalities [3–7]. Among such materials, molecule-based magnetic materials are promising candidates for multifunctional materials. In the last two decades, multifunctional molecule-based magnetic materials, which combine magnetic phenomena of long-range magnetic ordering, slow magnetic relaxation, or spin transition with another functionality, have been reported [8–12]. Two-dimensional (2D) and three-dimensional (3D) coordination compounds with strong magnetic coupling between spin centers can exhibit long-range magnetic ordering, whereas non-centrosymmetric compounds are expected to show magnetic circular dichroism (MCD), magneto-chiral dichroism (MChD), and nonlinear magneto-optical effects. In an oxalate-bridged Mn^{II}–Cr^{III} ferromagnetic network with chiral counterions, an enhanced MChD effect has been observed due to the long-range magnetic ordering below the Curie temperature (T_C) of 7 K [13]. An enhanced MCD effect has been realized in a cyanido-bridged Mn^{II}(L)–Cr^{III} ferrimagnet with $T_C = 38$ K (L = (*S*)-1,2-diaminopropane) [14] and a cyanido-bridged Mn^{II}(L′)–Nb^{IV} with $T_C = 23.5$ K ferrimagnet (L′ = (*S*/*R*)-α-methyl-2-pyridinemethanol) [15]. A few reports have introduced chirality in low-dimensional systems displaying slow magnetic relaxation [16, 17], and the MCD effect has been demonstrated for an Mn_6–[(*R*)-sao] cluster ((*R*)-sao = chiral salicylaldoxime derivative) [18]. As for other magneto-optical effects, second harmonic generation (SHG), which is a nonlinear optical effect, is considerably enhanced by the onset of long-range magnetic ordering. This effect, called magnetization-induced second harmonic generation (MSHG), has been reported in Co–Cr Prussian blue analogs [19, 20], a cyanido-bridged Mn–Nb ferrimagnet [21, 22], a cyanido-bridged Mn–Mo ferrimagnet [23], and a Mn–Cr oxalate ferromagnet [24].

Some molecule-based magnets display ferroelectricity and proton conduction. For example, ferroelectricity and ferromagnetism coexist in rubidium manganese hexacyanoferrate [25]. Prussian blue analogs of $Co[Cr(CN)_6]_{2/3}\cdot zH_2O$ and $V[Cr(CN)_6]_{2/3}\cdot zH_2O$ show a high proton conduction exceeding 10^{-3} S cm^{-1} [26]. Moreover, $V[Cr(CN)_6]_{2/3}$ with a high magnetic phase transition temperature of 313 K exhibits an interference effect between magnetic ordering and proton conduction, which is likely caused by the distortion of the 3D hydrogen bonding network by magnetostriction below the T_C.

Photoresponsive magnets with photomagnetism such as photoinduced magnetization are some of the most interesting materials [27–31]. A cyanido-bridged Co–W metal assembly, $[\{Co^{II}(4\text{-methylpyridine})(\text{pyrimidine})\}_2\{Co^{II}(H_2O)_2\}\{W^{V}(CN)_8\}_2]\cdot 4H_2O$, exhibits photoinduced ferromagnetic ordering with a high T_C of 48 K and a large magnetic coercive field (H_c) of 27,000 Oe [32]. These T_C and H_c values are the highest in photoinduced magnetization systems. Furthermore, in a chiral cyanido-bridged Fe–Nb assembly, (±)–$Fe_2[Nb(CN)_8](4\text{-bromopyridine})_8\cdot 2H_2O$, spin-crossover-induced SHG, light-reversible spin-crossover, long-range magnetic ordering, and photoswitching of MSHG have been observed [33].

Luminescent magnets are an attractive target in molecule-based materials. Molecule-based magnets often have a lighter color in the visible light region compared to that of conventional magnets composed of metal oxides and other inorganic compounds. Light color materials are preferable for efficient luminescence in

the visible light region. To date, some molecule-based magnetic compounds have been reported [34, 35].

23.2 Photomagnets and First-Principles Calculations

Numerous studies on optically switchable materials have been conducted toward applications as optical memory devices. Examples reported to date include metal oxides, photochromic compounds, chalcogenides, spin-crossover complexes, and cyanido-bridged metal assemblies. Cyanido-bridged Co–W metal assemblies are known to exhibit photoinduced ferromagnetism with a high T_C and H_c [30–32]. This phenomenon is attributed to an optical charge-transfer-induced spin transition (CTIST) from the Co^{III} (low spin, $S = 0$)–W^{IV}($S = 0$) phase to the Co^{II} (high spin, $S = 3/2$)–W^{V}($S = 1/2$) phase. However, the electronic structure of the optical transition and the mechanism for photomagnetic effects remain unclear.

A recent study revealed the electronic structure of a 2D cyanido-bridged Co–W metal assembly, $(H_5O_2^+)[Co(4\text{-bromopyridine})_2\{W(CN)_8\}]$ [36]. Figure 23.1 shows the crystal structure of the cyanido-bridged Co–W metal assembly. The Co–N distances at the axial positions coordinated by 4-bromopyridine are 1.96–1.97 Å longer than those at equatorial positions coordinated by cyanide (1.88–1.91 Å). The average distance of 1.92 Å indicates trivalent Co ions. As a specific character, this Co–W metal assembly possesses $H_5O_2^+$ ions. Thus, the assembly is exposed to an acidic circumstance of $H_5O_2^+$ ions even in the solid state. The presence of IR peaks due to O–H^+–O groups at 930, 1090, 1310, 1400, and 1720 cm^{-1} confirms the existence of $H_5O_2^+$ ions. The blue crystal of the Co–W metal assembly shows an optical absorption band around 1.8 eV (700 nm), which is derived from Co^{III}. The magnetic susceptibility measurement demonstrates that the value is almost zero, revealing the electronic state of Co^{III}_{ls} ($S = 0$)–W^{IV} ($S = 0$) is between 2 and 390 K. This is a first example where the Co^{III}_{ls} ($S = 0$)–W^{IV} ($S = 0$) state appears over a wide temperature range between 2 and 390 K. This is because the $[W(CN)_8]^{4-}$ ion is more stable under acidic conditions.

First principles calculations reveal the optical transitions in $(H_5O_2^+)[Co(4\text{-bromopyridine})_2\{W(CN)_8\}]$. The periodic structure calculation was conducted based on the crystal structure determined by single-crystal X-ray diffraction analysis. Figure 23.2 shows the band structure and the density of states. The top of the valence band just below the Fermi energy (E_F) is mainly composed of W^{IV} and N states. The bottom of the conduction band just above E_F consists of Co^{III} and N states. The calculated optical absorption spectrum reproduces the observed spectrum well (Fig. 23.2b). As shown in Fig. 23.2c, the lowest-energy transition is from the valence band mainly containing the d_{z2} orbitals of W^{IV} and the p orbitals of N to the conduction band mainly derived from the d_{z2} orbitals of Co^{III} and the sp orbitals of N. Bader analysis provides charge density distributions of Co 0%, W 63%, N 36%, and C 0% for the valence band and Co 63%, W 1%, N 29%, and C 5% for the conduction band, indicating that the charge transfer from W^{IV} to Co^{III} is the lowest energy transition.

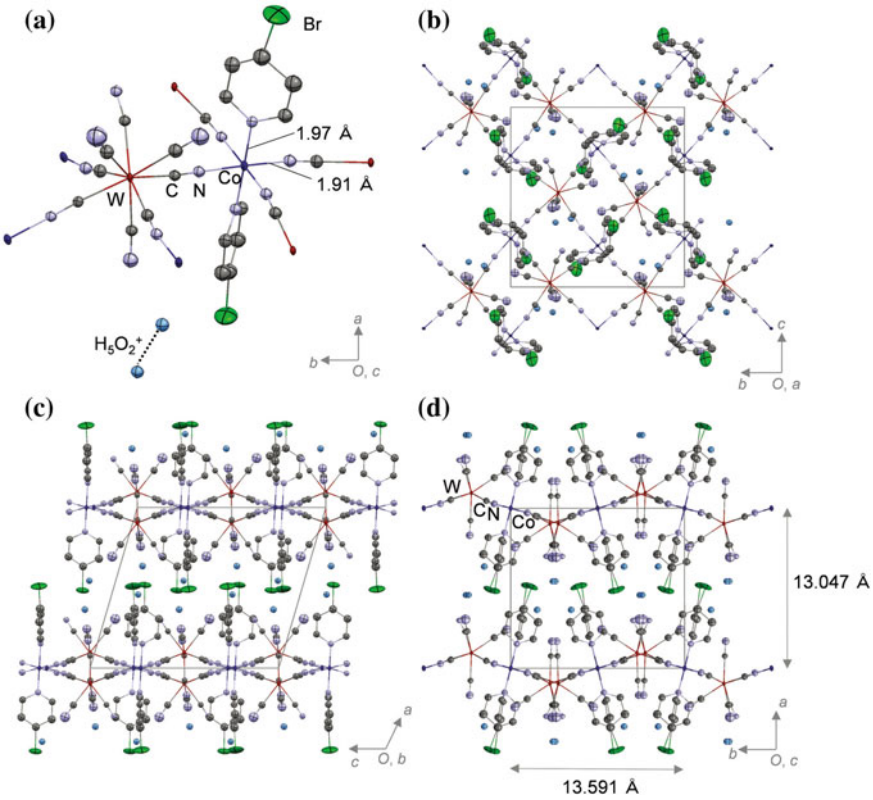

Fig. 23.1 Crystal structure of the two-dimensional cyanido-bridged Co–W metal assembly, $(H_5O_2^+)[Co(4\text{-bromopyridine})_2\{W(CN)_8\}]$. **a** Coordination geometry around Co and W. Views along **b** the a-axis, **c** the b-axis, and **d** the c-axis. Red, blue, light purple, gray, light blue, and green ellipsoids indicate W, Co, N, C, O, and Br, respectively. Hydrogen atoms are omitted for clarity. Reproduced from [36] with permission from the Royal Society of Chemistry

In addition, the charge density of the N atoms is considerably large, suggesting it contributes to the transition. Considering the orbital angular momentum and the parity of the p and sp orbitals, the transition from p to sp is allowed. Consequently, the charge transition process is accelerated through the orbitals of the bridging cyanides.

The photoresponsivity of the Co–W metal assembly was studied. Irradiating the assembly with a 785-nm CW laser light at 240 mW cm^{-2} and 4 K decreases the optical absorption around 1.8 eV (700 nm) and causes an absorption around 2.3 eV (540 nm), which is assigned to a charge transfer band from Co^{II} to W^{V} (Fig. 23.3). Thus, the photoirradiation induces a charge transfer phase transition from Co^{III}–W^{IV} to Co^{II}–W^{IV} phases with a drastic color change from blue to red. The phase transition provides a drastic change of magnetic properties. Additionally, irradiation with 785-nm light (220 mW m^{-2}) at 3 K induces spontaneous magnetization with T_C of 27 K, as shown in the magnetization (M) versus temperature (T) plots (Fig. 23.4).

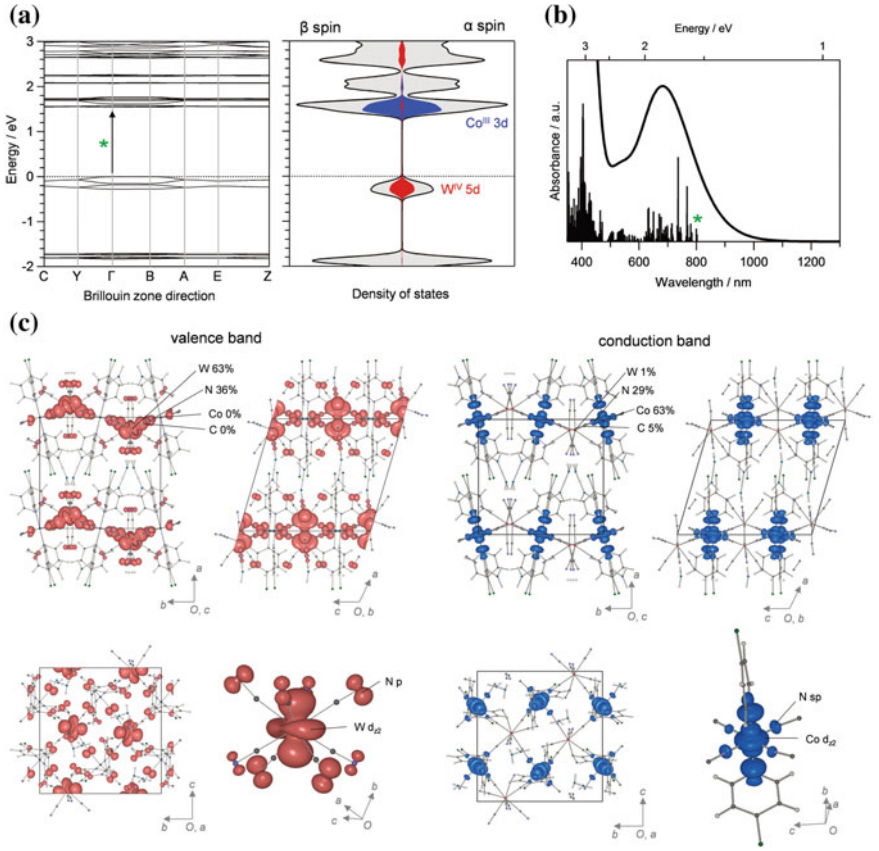

Fig. 23.2 First-principles calculations for $(H_5O_2^+)[Co(4\text{-bromopyridine})_2\{W(CN)_8\}]$. **a** Band structure (left) and density of states (DOS) near the Fermi energy level (right). Red, blue, and gray areas show the partial DOS for W^{IV} 5d, Co^{III} 3d, and the total DOS, respectively. **b** Calculated optical absorption spectrum. Black bars represent the calculated absorption strengths, while the line with an asterisk denotes the lowest-energy transition. **c** Charge density maps of the valence (left) and the conduction (right) bands. Reproduced from [36] with permission from the Royal Society of Chemistry

The M versus external magnetic field (H) plot after photoirradiation shows a coercive field of 2000 Oe at 2 K and a magnetization value of 3.0 μ_B at 50 kOe. The observed magnetization value almost agrees with the expected saturation magnetization value assuming ferromagnetic coupling between Co^{II} ($S = 1/2$, $g = 13/3$) and W^V ($S = 1/2$, $g = 2$). The photoinduced phase relaxes to the initial phase upon heating. These photothermal changes are reversible.

The powder XRD measurements before and after photoirradiation and their Rietveld analyses reveal the crystal structure of the photoinduced phase. The lattice constants increase by 3% in the 2D layer corresponding to the *bc*-plane compared to

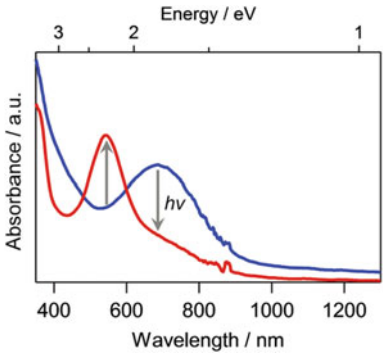

Fig. 23.3 UV-vis spectra of $(H_5O_2^+)[Co(4\text{-bromopyridine})_2\{W(CN)_8\}]$ before (blue line) and after photoirradiation (red line). Reproduced from [36] with permission from the Royal Society of Chemistry

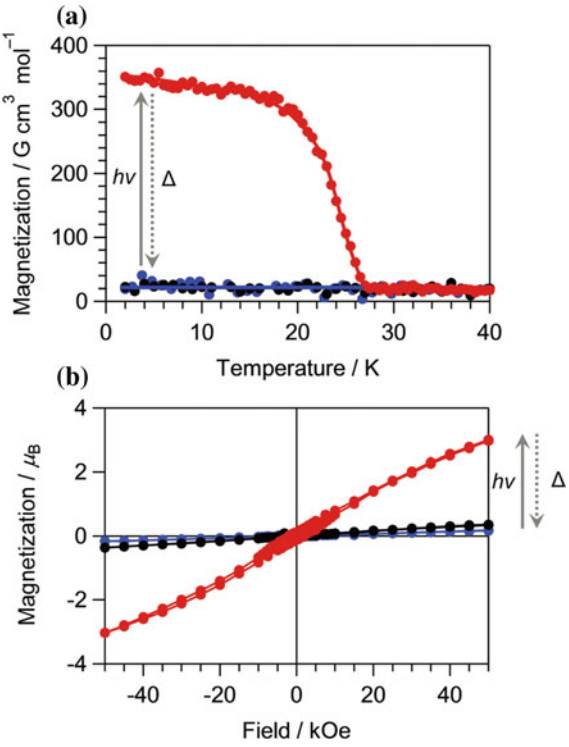

Fig. 23.4 Magnetic properties of $(H_5O_2^+)[Co(4\text{-bromopyridine})_2\{W(CN)_8\}]$ before (blue line), after photoirradiation (red line), and after heating up to 80 K (black). **a** *M*-*T* plots, **b** *M*-*H* plots. Reproduced from [36] with permission from the Royal Society of Chemistry

those of the original phase. The Co–N average distance of 2.05 Å, which is longer than that of the original phase (1.92 Å), indicates that photoirradiation changes the valence state from Co^{III} to Co^{II}. By increasing the temperature up to 60 K, the crystal structure of the photoinduced phase returns to that of the original phase. Among cyanido-bridged Co–W photomagnets, this is the first example where the crystal structure of the photoinduced phase is determined.

In another embodiment of photomagnetism for cyanido-bridged metal assemblies, a Cu–Mo metal assembly of $\{[Cu^{II}(H_2O)]_2[Mo^{IV}(CN)_8]\}\cdot 2H_2O$ was studied [37]. This compound is a known photomagnet, but until recently its crystal and electronic structures, which are necessary to discuss the optical transitions and the mechanism of photomagnetic effects, were unclear. Improving the crystallinity of the Cu–Mo metal assembly by using a gel method allows single-crystal XRD analysis, revealing the 3D cyanido-bridged Cu–Mo framework (Fig. 23.5). Based on this crystal structure, first-principles calculations of the Cu–Mo metal assembly were performed.

In the calculations, a primitive unit cell with a $\{Cu_4Mo_2C_{16}N_{16}H_{16}O_8\}$ composition composed of two stoichiometric $\{Cu_2MoC_8H_8N_8O_4\}$ molecular fragments, was used. The Cu^{II} 3p/3d electrons, the Mo^{IV} 4p/4d electrons, the O 2p electrons, the H 1s electrons, and the CN– 2p electrons were considered, resulting in a total of 300 occupied bands. Half of the bands are occupied by α spins (1st to 150th valence bands: v1α–v150α), while the other half are occupied by β spins (1st to 150th valence

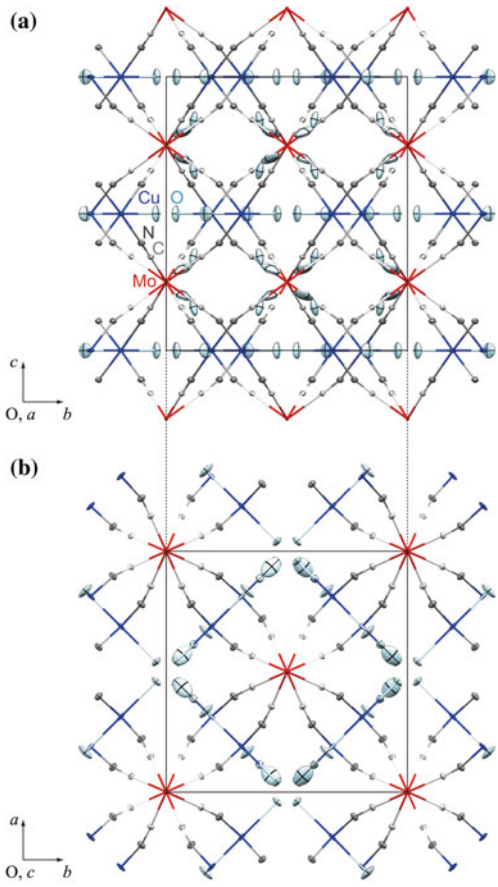

Fig. 23.5 Crystal structure of the 3D cyanido-bridged Cu–Mo metal assembly, $\{[Cu^{II}(H_2O)]_2[Mo^{IV}(CN)_8]\}\cdot 2H_2O$, along **a** the *a* axis and **b** the *c* axis. Red, blue, dark gray, gray, and light blue ellipsoids indicate Mo, Cu, N, C, and O, respectively. Hydrogen atoms are omitted for clarity. Reproduced from [37] with permission from John Wiley and Sons

bands: v1β–v150β). Figure 23.6 shows the calculated total and partial DOS in the range from –4 to 4 eV, where the occupied bands below E_F as well as the unoccupied bands in an area just above E_F (the conduction bands for or spins from c1α/β to c12α/β) are presented. The occupied bands just below the E_F level (v1α/β and v2α/β) mainly consist of the Mo^{IV} states, whereas the unoccupied bands just above the E_F level (c1α/β and c2α/β) are composed of the Cu^{II} states. The contributions from the nitrogen, carbon, and oxygen atoms exist in the valence bands below –1 eV and the conduction bands above +1.2 eV. Figure 23.7 shows the details about the band structure near the E_F level. The optical transition of the band gap is a direct transition with a band gap of 1.2 eV exactly at the point corresponding to the transition between the occupied v1α band and the unoccupied c1α band.

Figure 23.7b depicts the charge density maps for the v1α and c1α bands, indicating that the Mo^{IV} d_{z2} orbital and the N p_z orbital mainly contribute to the valence band of v1α. The conduction band of c1α is formed mostly by the Cu^{II} d_{x2-y2} orbital with an admixture of the N sp_x orbitals. Bader analysis gives charge density distributions with Cu 1.52%, Mo 63.96%, C 0.00%, and N 34.44% for the top of the valence band and Cu 68.14%, Mo 5.48%, C 8.76%, and N 17.60% for the bottom of the conduction band. Similar to the Co–W system mentioned above, the contribution of the nitrogen orbitals is significant for the charge transfer in the Cu–Mo system because the transition from p to sp is an allowed transition. Thus, the charge transfer from Mo^{IV} to Cu^{II} is enhanced through the orbitals of the nitrogen atoms in the bridging cyanides. The electronic structure produces the calculated UV-vis absorption spectrum (Fig. 23.8). The visible-range absorption is due to the optical transitions from the valence bands of v1α/β and v2α/β composed mainly of the Mo^{IV} orbitals to the conduction bands of c1α/β and c2α/β composed mainly of the Cu^{II} orbitals. The absorption in the UV range is derived from metal-to-ligand charge transfer (MLCT) from the Mo^{IV} to the cyanido ligand, the d-d transition in Mo^{IV}, and the ligand-to-metal charge transfer (LMCT) from the cyanido ligand to the Cu^{II}. These results demonstrate that visible-light irradiation causes a transition from the v1α to the c1α/β, that is, a charge transfer from Mo^{IV} to Cu^{II}. This supports a mechanism of photoinduced charge transfer in Cu–Mo systems, as reported previously.

23.3 Luminescent Magnetic Materials

The combination of luminescence and magnetic properties is an interesting topic in the field of molecule-based materials. To construct switchable luminescent magnets, building blocks of Ln^{III}, organic ligands, and cyanide metallates were selected. Lanthanide (3+) can act as luminophore and spin source. Organic ligands are luminophores and photosensitizers that induce energy transfer from an organic ligand towards Ln^{III}. A cyanido-bridged Tb^{III}(Box)–W^{V} metal assembly, $\{[Tb^{III}(Box)_2(dmf)_2]–[W^{V}(CN)_8]\}\cdot H_2O$ (Box = 2,2′-Bis(2-oxazoline), dmf = *N*,*N*′-dimethylformamide), was prepared by mixing solutions of the building blocks [38]. Figure 23.9 shows the crystal structure of the compound, revealing a 2D cyanido-

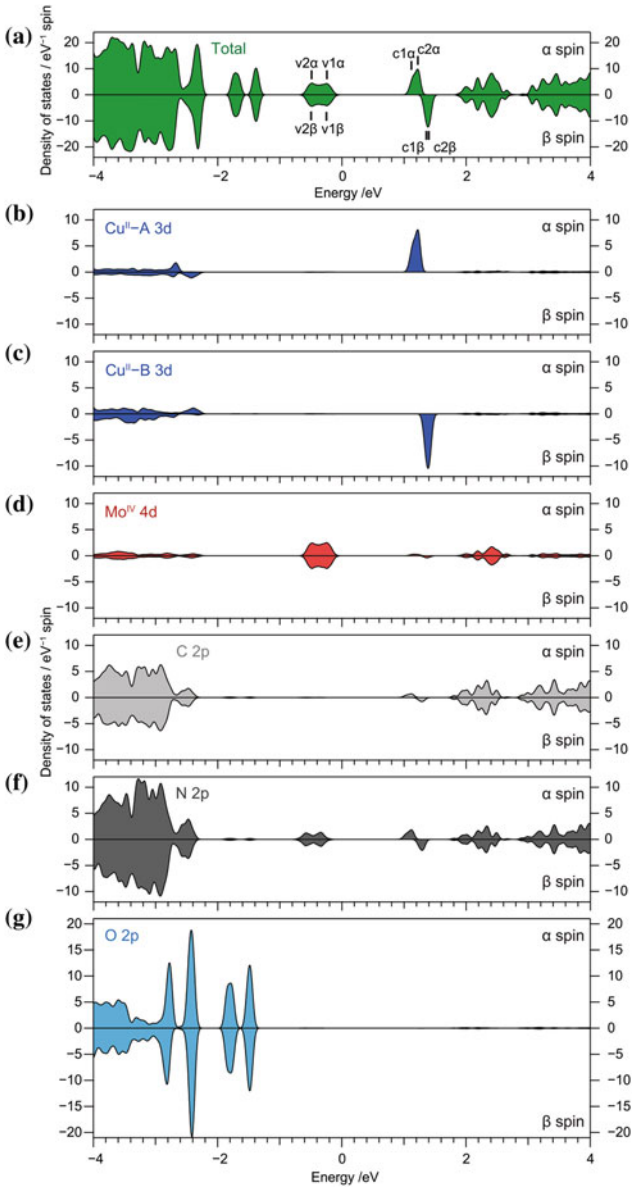

Fig. 23.6 Total and partial DOS of $\{[Cu^{II}(H_2O)]_2[Mo^{IV}(CN)_8]\}\cdot 2H_2O$. Cu^{II}–A and Cu^{II}–B represent two possible positions of Cu^{II} in the crystal structure. v1α/β and v2α/β show the first and second-highest valence bands for α or β spin, respectively. c1α/β and c2α/β indicate the first and second-highest conduction bands for α or β spin, respectively. Reproduced from [37] with permission from John Wiley and Sons

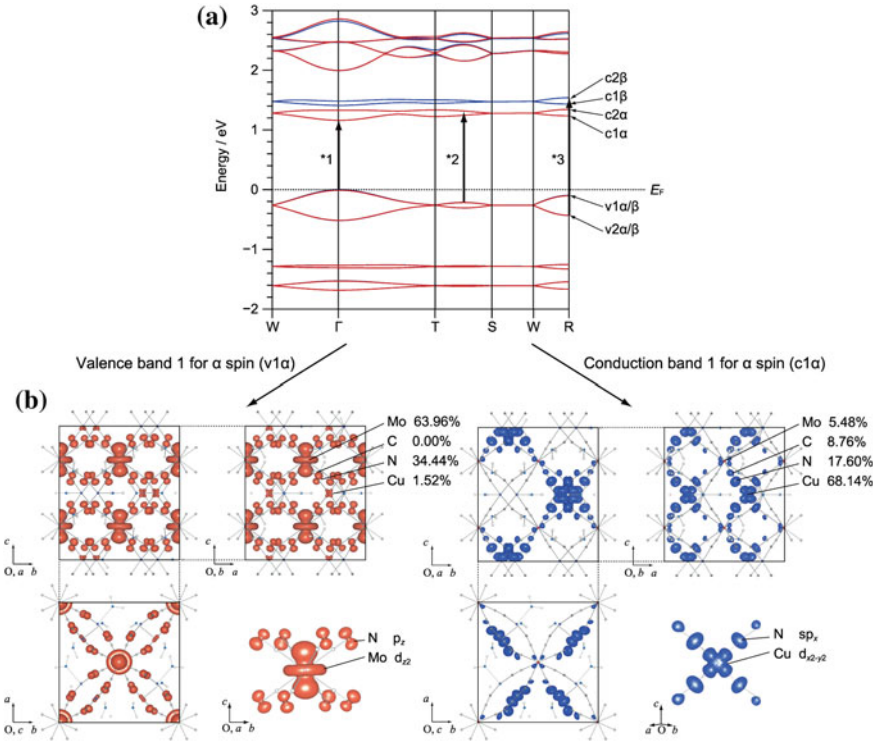

Fig. 23.7 **a** Band structure of $\{[Cu^{II}(H_2O)]_2[Mo^{IV}(CN)_8]\}\cdot 2H_2O$ near the E_F level. Red and blue lines represent α and β spin, respectively. Black arrows of *1, *2, and *3 indicate three selected transitions from the valence to the conductions bands at various *k* points, corresponding to three component lines in the calculated UV/Vis spectrum (Fig. 23.9b). **b** Charge-density maps for the bottom of the conduction band (c1α at the Γ point, top) and the top of the valence band (v1α at the Γ point, bottom) with the charge density around the metal centers. Reproduced from [37] with permission from John Wiley and Sons

bridged Tb^{III}(Box)–W^V network. The direct-current (dc) magnetism reveals a long-range magnetic ordering below T_C of 2.4 K. The magnetization vs. external magnetic field at 1.8 K suggests ferromagnetic interactions between Tb^{III} and W^V.

The solid-state luminescence properties were studied by measuring the emission and excitation spectra at 77 K (Fig. 23.10). The compound exhibits two different luminescent colours depending on the wavelength of the UV excitation. Irradiating with 260-nm excitation light provides an emission spectrum with strong sharp peaks at 490, 545, 585, and 622 nm and weaker peaks at 647, 667, and 678 nm, resulting in green luminescence. This emission is attributed to intra f^8 $^5D_4 \rightarrow {}^7F_{0\text{-}6}$ transitions in Tb^{III}. Irradiating with 340-nm light induces a dominant broad band at 650 nm and a weak broad band at 435 nm that are accompanied by the weak peaks of Tb^{III} center luminescence. The dominant broad emission produces red luminescence.

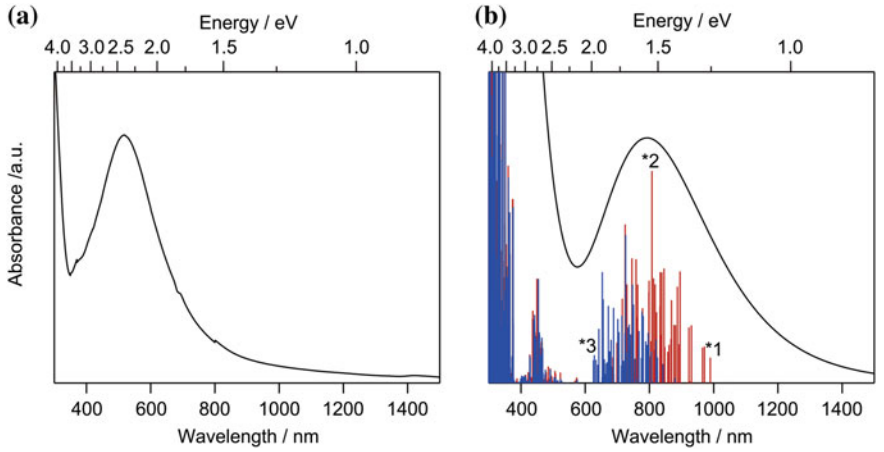

Fig. 23.8 **a** Experimental and **b** calculated UV/Vis spectrum of $\{[Cu^{II}(H_2O)]_2[Mo^{IV}(CN)_8]\}\cdot 2H_2O$. Red and blue lines indicate the calculated absorption strengths of the α and β spin bands, respectively. Reproduced from [37] with permission from John Wiley and Sons

The emission at 650 nm is assigned to $^3(\pi - \pi^*)T_1 \rightarrow S_0$ phosphorescence of the Box ligand. Since Box alone does not exhibit phosphorescence but instead shows the blue fluorescence of the $^1(\pi - \pi^*)S_1 \rightarrow S_0$ transition, the phosphorescence is due to the heavy atom effect of Tb^{III} accelerating the $S_1 \rightarrow T_1$ intersystem crossing followed by the $T_1 \rightarrow S_0$ transition. Thus, irradiating this compound with UV light below 300 nm only populates the excited states of Tb^{III} because Box does not possess such high energy levels. As a result, a green emission is observed. On the contrary, UV light above 300 nm provides both excited states of Tb^{III} and Box. Energy transfer efficiently occurs to the T_1 state of Box, leading to a red emission.

A cyanido-bridged Dy^{III}–Co^{III} metal assembly, $\{[Dy^{III}(3\text{-hydroxypyridine})_2(H_2O)_4][Co^{III}(CN)_6]\cdot H_2O\}$, was prepared [39], and single-crystal XRD analysis revealed a zig-zag chain structure (Fig. 23.11). The alternate-current (ac) susceptibility measurements show a SMM behavior of the intrachain Dy complexes, and analyses using the generalized Debye model give a thermal energy barrier of ΔE of 266(12) cm^{-1} with a relaxation time τ_0 of $3.2(2) \times 10^{-11}$ s. This is one of the largest energy barriers among emissive SMMs. Below 10 K, the $\ln\tau$ versus T^{-1} plot becomes temperature-independent due to the significant quantum tunneling of magnetization (QTM) effect (Fig. 23.12). The QTM is partially suppressed by applying external magnetic fields of 1 and 2 kOe. Due to the high ΔE, magnetization hysteresis loops are observed below 6 K for a field sweep rate of 10 Oe/s. The QTM effect dominating at low magnetic fields and temperatures may lead to the characteristic butterfly shape of the M-H loops.

The cyanido-bridged Dy^{III}–Co^{III} metal assembly shows a white light emission when excited by 312 nm light (Fig. 23.13). The emission spectrum with 481, 576,

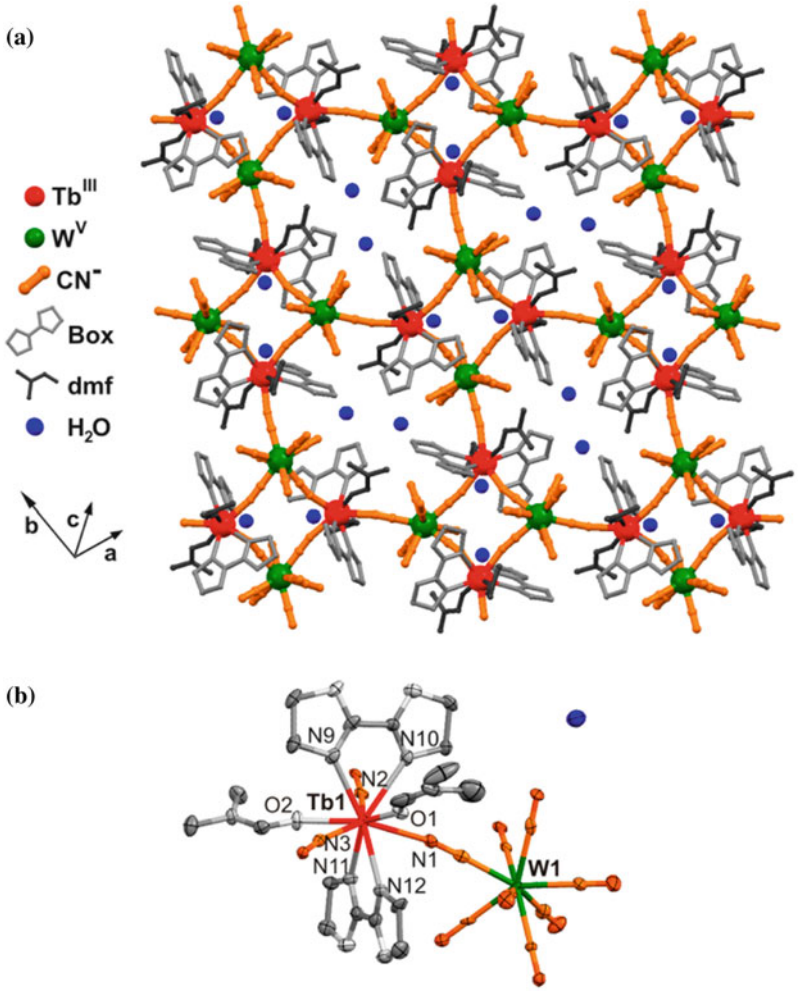

Fig. 23.9 Crystal structure of the two-dimensional cyanido-bridged Tb–W metal assembly, $\{[Tb^{III}(Box)_2(dmf)_2]–[W^V(CN)_8]\}\cdot H_2O$. **a** 2D structure and **b** the coordination geometry around Tb^{III} and W^V. Hydrogen atoms are omitted for clarity. Adapted with permission from [38]. Copyright 2014 American Chemical Society

and 660 nm is assigned to $^4F_{9/2} \rightarrow {}^6H_{15/2,13/2,11/2}$ transitions on Dy^{III}. In the excitation spectrum, the broad band at 312 nm, which is assigned to 3-hydroxypyridine and $[Co^{III}(CN)_6]^{3-}$, is predominant, indicating an energy transfer from the organic ligand and Co^{III} to Dy^{III}. At a low temperature of 3.5 K, a high-resolution emission spectrum was rather collected, and it can be deconvoluted into eight components, which are considered to be the crystal field splitting of $^6H_{15/2}$ multiples. The energy difference between the two lowest doublets is 211(31) cm^{-1}. This energy corresponds to the

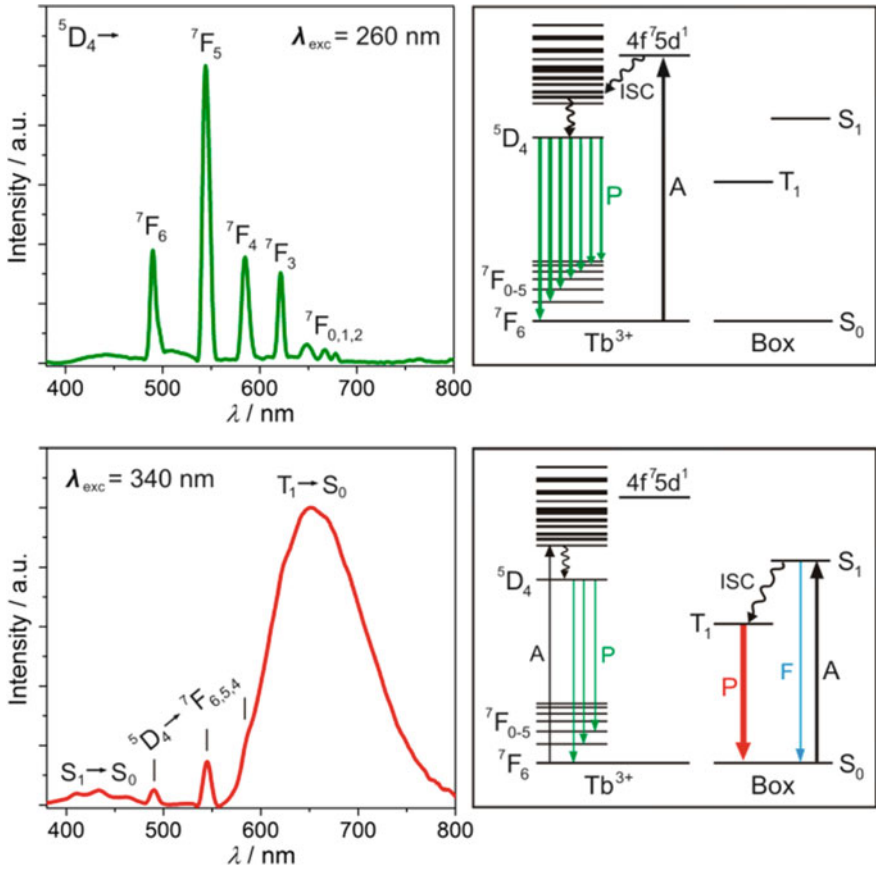

Fig. 23.10 Emission spectra of $\{[Tb^{III}(Box)_2(dmf)_2]$–$[W^V(CN)_8]\}\cdot H_2O$ at $T = 77$ K excited by 260 nm (upper left) and 340 nm (bottom left) light. Right schematic illustration represents the energy level diagrams with electronic transitions. A = absorption, P = phosphorescence, F = fluorescence, ISC = intersystem crossing. Reprinted with permission from [38].

zero-field energy barrier, which is close to the value of 266(12) cm^{-1} estimated from the magnetic analysis mentioned above. The cyanido-bridged Dy^{III}–Co^{III} metal assembly is a unique multifunctional material exhibiting a white light emission and SMM behavior.

This chapter presents recent examples of multifunctional cyanido-bridged metal assemblies exhibiting photomagnetism or luminescence. Although the aforementioned Co^{II}–W^V and Cu^{II}–Mo^{IV} metal assemblies have well known photomagnetism, the electronic structures were not clear. Recently, first principles calculations have revealed their electronic structures. This knowledge will allow researchers to design new photomagnets with higher functionalities. The combination of luminescence and long-range magnetic ordering (or single-molecule magnetic behavior) is a sophis-

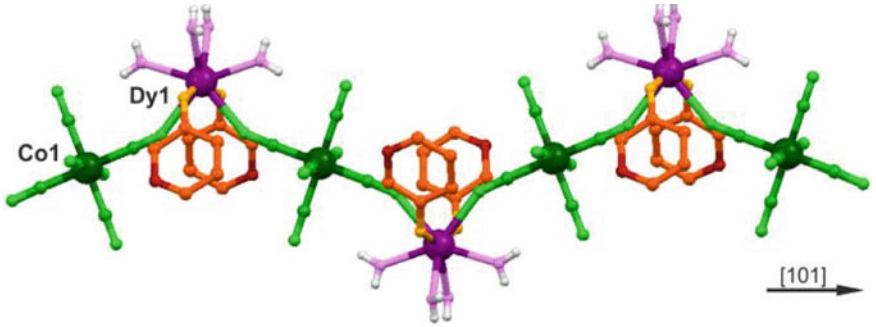

Fig. 23.11 Zig-zag chain structure of {[Dy^{III}(3-hydroxypyridine)$_2$(H_2O)$_4$][Co^{III}(CN)$_6$]·H_2O} revealed by single-crystal XRD. Reproduced from [39] with permission from John Wiley and Sons

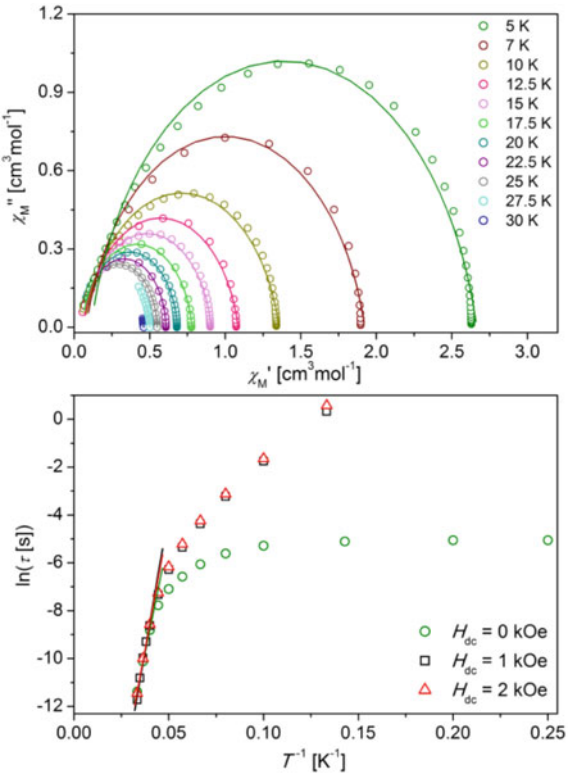

Fig. 23.12 Alternate-current (ac) magnetism of {[Dy^{III}(3-hydroxypyridine)$_2$(H_2O)$_4$][Co^{III}(CN)$_6$]·H_2O}: the $\chi_{M''} - \chi_{M'}$ plots at indicated T (upper) and the relaxation time (τ) as ln(τ) versus T^{-1} plots in various H_{dc} of 0, 1, and 2 kOe. Solid lines in the upper figure are fitted using the generalized Debye model, whereas the lines in the bottom figure are fitted to the Arrhenius law. Reproduced from [39] with permission from John Wiley and Sons

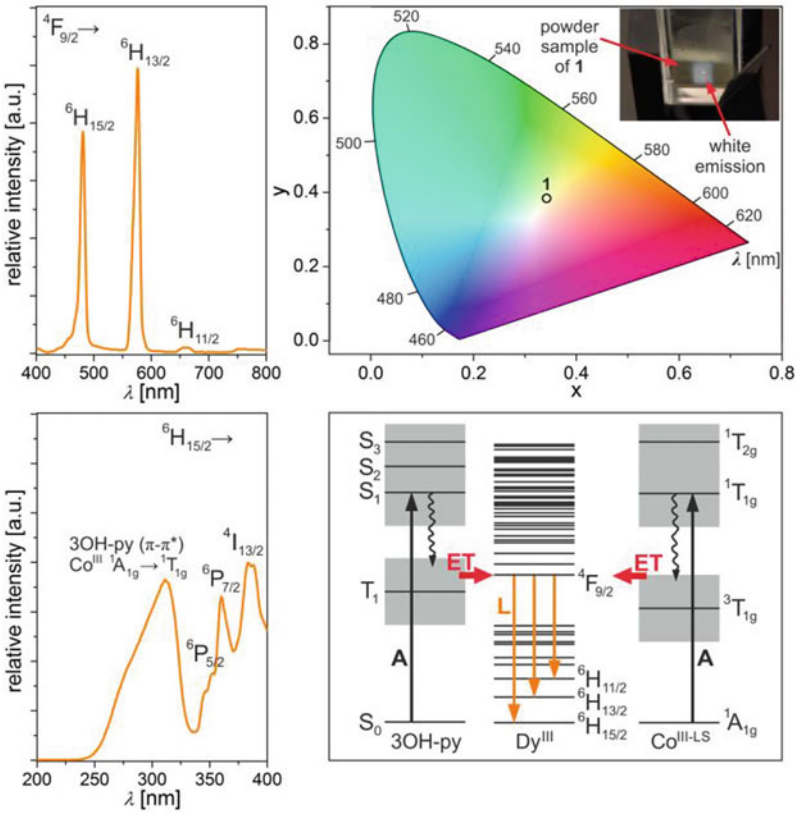

Fig. 23.13 Solid state emission (upper left, $\lambda_{exc} = 312$ nm) and excitation (bottom left, $\lambda_{em} = 576$ nm) spectra of $\{[Dy^{III}(3\text{-hydroxypyridine})_2(H_2O)_4][Co^{III}(CN)_6]\cdot H_2O\}$, 1, at $T = 300$ K. Emission color is presented on the CIE 1931 chromaticity diagram (upper right). Inset shows the photo of the white emission from the powder sample. Related energy level diagram is presented (bottom right; A = absorption, ET = energy transfer, L = lanthanide luminescence). Reproduced from [39] with permission from John Wiley and Sons

ticated functionality for molecule-based materials and should inspire new ideas in related research areas.

References

1. A.K.T. Lau, J. Lu, V.K. Varadan, F.K. Chang, J.P. Tu, P.M. Lam, *Multi-functional Materials and Structures* (Trans Tech Publications, Hong Kong, 2008)
2. S.M. Mukhopadhyay, *Nanoscale Multifunctional Materials: Science and Applications* (Wiley, New Jersey, 2012)
3. H. Tokoro, S. Ohkoshi, Dalton Trans. **40**, 6825 (2011)
4. E. Coronado, C. Gimnez-Saiz, C. Marti-Gastaldo, *Engineering of Crystalline Materials Properties*, ed. by J.J. Novoa, D. Braga, L. Addadi (Springer, Dordrecht, 2008), pp. 173
5. D. Maspoch, D. Ruiz-Molina, J. Veciana, Chem. Soc. Rev. **36**, 770 (2007)
6. P. Dechambenoit, J.R. Long, Chem. Soc. Rev. **40**, 3249 (2011)
7. M.D. Allendorf, C.A. Bauer, R.K. Bhakta, R.J.T. Houk, Chem. Soc. Rev. **38**, 1330 (2009)
8. S. Ohkoshi, H. Tokoro, Acc. Chem. Res. **45**, 1749 (2012)
9. E. Coronado, D. Gatteschi, J. Mater. Chem. **16**, 2513 (2006)
10. H. Tokoro, S. Ohkoshi, Bull. Chem. Soc. Jpn. **88**, 227 (2015)
11. O. Kahn, O. Cador, J. Larionova, C. Mathoniere, J.-P. Sutter, Mol. Cryst. Liq. Cryst. Sci. Technol. Sect. A **305**(1) (1997)
12. C. Train, M. Gruselle, M. Verdaguer, Chem. Soc. Rev. **40**, 3297 (2011)
13. C. Train, R. Gheorghe, V. Krstic, L.-M. Chamoreau, N.S. Ovanesyan, G.L.J.A. Rikken, M. Gruselle, M. Verdaguer, Nat. Mater. **7**, 729 (2008)
14. K. Inoue, K. Kikuchi, M. Ohba, H. Okawa, Angew. Chem. Int. Ed. **42**, 4810 (2003)
15. S. Chorazy, R. Podgajny, W. Nitek, T. Fic, E. Gçrlich, M. Rams, B. Sieklucka, Chem. Com-mun. **49**, 6731 (2013)
16. S. Chorazy, K. Nakabayashi, K. Imoto, J. Mlynarski, B. Sieklucka, S. Ohkoshi, J. Am. Chem. Soc. **134**, 16151 (2012)
17. J. Ferrando-Soria, D. Cangussu, M. Eslava, Y. Journaux, R. Lescouézec, M. Julve, F. Lloret, J. Pasan, C. Ruiz-Perez, E. Lhotel, C. Paulsen, E. Pardo, Chem. Eur. J. **17**, 12482 (2011)
18. J.M. Bradley, A.J. Thomson, R. Inglis, C.J. Milios, E.K. Brechin, S. Piligkos, Dalton Trans. **39**, 9904 (2010)
19. T. Nuida, T. Matsuda, H. Tokoro, S. Sakurai, K. Hashimoto, S. Ohkoshi, J. Am. Chem. Soc. **127**, 11604 (2005)
20. S. Ohkoshi, K. Arai, Y. Sato, K. Hashimoto, Nat. Mater. **3**, 857 (2004)
21. Y. Tsunobuchi, W. Kosaka, T. Nuida, S. Ohkoshi, Cryst. Eng. Comm. **11**, 2051 (2009)
22. D. Pinkowicz, R. Podgajny, W. Nitek, M. Rams, A.M. Majcher, T. Nuida, S. Ohkoshi, B. Sieklucka, Chem. Mater. **23**, 21 (2011)
23. M. Komine, K. Imoto, Y. Miyamoto, K. Nakabayashi, S. Ohkoshi, Eur. J. Inorg. Chem., 1367 (2018)
24. C. Train, T. Nuida, R. Gheorghe, M. Gruselle, S. Ohkoshi, J. Am. Chem. Soc. **131**, 16838 (2009)
25. E. Pardo, C. Train, H. Liu, L.M. Chamoreau, B. Dhkil, K. Boubekeur, F. Lloret, K. Nakatani, H. Tokoro, S. Ohkoshi, M. Verdaguer, Angew. Chem. Int. Ed. **51**, 8356 (2012)
26. S. Ohkoshi, H. Tokoro, T. Matsuda, H. Takahashi, H. Irie, K. Hashimoto, Angew. Chem. Int. Ed. **46**, 3238 (2007)
27. S. Ohkoshi, K. Imoto, Y. Tsunobuchi, S. Takano, H. Tokoro, Nat. Chem. **3**, 564 (2011)
28. E.S. Koumousi, I.-R. Jeon, Q. Gao, P. Dechambenoit, D.N. Woodruff, P. Merzeau, L. Buisson, X. Jia, D. Li, F. Volatron, C. Mathonière, R. Clérac, J. Am. Chem. Soc. **136**, 15461 (2014)
29. O.N. Risset, P.A. Quintero, T.V. Brinzari, M.J. Andrus, M.W. Lufaso, M.W. Meisel, D.R. Talham, J. Am. Chem. Soc. **136**, 15660 (2014)
30. S. Ohkoshi, Y. Hamada, T. Matsuda, Y. Tsunobuchi, H. Tokoro. Chem. Mater. **20**, 3048 (2008)
31. S. Ohkoshi, S. Ikeda, T. Hozumi, T. Kashiwagi, K. Hashimoto, J. Am. Chem. Soc. **128**, 5320 (2006)
32. N. Ozaki, H. Tokoro, Y. Hamada, A. Namai, T. Matsuda, S. Kaneko, S. Ohkoshi, Adv. Funct. Mater. **22**, 2089 (2012)

33. S. Ohkoshi, S. Takano, K. Imoto, M. Yoshikiyo, A. Namai, H. Tokoro, Nat. Photonics **8**, 65 (2014)
34. J.-M. Rueff, J.-F. Nierengarten, P. Gillot, A. Demessence, O. Cregut, M. Drillon, P. Ra-bu, Chem. Mater. **16**, 2933 (2004)
35. E. Chelebaeva, J. Larionova, Y. Guari, R.A.S. Ferreira, L.D. Carlos, F.A. Almeida Paz, A. Trifonov, C. Guerin, Inorg. Chem. **48**, 5983 (2009)
36. Y. Miyamoto, T. Nasu, N. Ozaki, Y. Umeta, H. Tokoro, K. Nakabayashi, S. Ohkoshi, Dalton Trans. **45**, 19249 (2016)
37. Y. Umeta, S. Chorazy, K. Nakabayashi, S. Ohkoshi, Eur. J. Inorg. Chem., 1980 (2016)
38. S. Chorazy, K. Nakabayashi, S. Ohkoshi, B. Sieklucka, Chem. Mater. **26**, 4072 (2014)
39. S. Chorazy, M. Rams, K. Nakabayashi, B. Sieklucka, S. Ohkoshi, Chem. Eur. J. **22**, 7371 (2016)